ARTICLES

Lower mantle heterogeneity, dynamic topography and the geoid

Bradford H. Hager, Robert W. Clayton, Mark A. Richards, Robert P. Comer[*] & Adam M. Dziewonski[*]

Seismological Laboratory, California Institute of Technology, Pasadena, California 91125, USA

Density contrasts in the lower mantle, inferred using seismic tomography, drive viscous flow; this results in kilometres of dynamically maintained topography at the core-mantle boundary and at the Earth's surface. The total gravity field due to interior density contrasts and dynamic boundary topography predicts the longest-wavelength components of the geoid remarkably well. Neglecting dynamic surface deformation leads to geoid anomalies of opposite sign to those observed.

THE LONGEST-WAVELENGTH components of the Earth's gravity field have been known for more than two decades from satellite geodesy[1,2] but there have been few observational constraints on the density anomalies causing them. Developments in seismology and theoretical geodynamics, until recently separate branches of geophysics, give new insight into this classical problem.

Seismological studies of lateral heterogeneity have determined the longest-wavelength components of seismic velocity variations in the lower mantle[3-6]. These velocity variations presumably would be proportional to density variations if both were the result of temperature differences associated with mantle convection. But these inferred density variations are, in fact, negatively correlated with the observed geoid, apparently contradicting the convection hypothesis.

Geodynamic theories of the Earth's gravity field show, however, that a negative correlation is not unexpected in a convecting Earth, because of the counteracting effects of dynamically supported surface deformations on the gravity field[7]. For example, hot upwellings in the mantle cause uplift of the Earth's surface and of the core-mantle boundary. This dynamically maintained topography has a strong effect on the gravity field. For a given interior density structure, the total gravity field (including the effects of surface deformation) depends on the viscosity structure and on the presence or absence of chemical stratification in the mantle[8,9].

Our main conclusion is that the longest-wavelength components of the residual geoid can be predicted from the seismically-inferred density contrasts in the lower mantle using dynamic response functions for mantle convection with a moderate increase in viscosity with depth. The inferred long-wavelength temperature differences are of the order of ±20 °C, with hot lower mantle underlying hotspot provinces at the Earth's surface. The inferred deformation of the core-mantle boundary is ~3 km.

It is possible to predict accurately the longest-wavelength geoid using the lower mantle seismic results and mantle flow models which include the effects of possible chemical stratification at the 670-km seismic discontinuity or with models which assume mantle-wide flow. Mantle-wide flow and stratified flow can, in principle, be distinguished on the basis of predicted dynamic topography at the Earth's surface. This dynamic topography, of the order of 1 km, is of opposite sign for the two styles of flow. Although incomplete knowledge of global dynamic topography and possible masking effects of dynamic topography because of upper mantle heterogeneities complicate interpretation, approximate agreement between model predictions and observations of topographic anomalies is suggestive of mantle-wide convection.

Seismic velocity structure

We describe here two independent methods to invert similar International Seismological Centre (ISC) P-wave travel-time residual data sets for the velocity structure of the lower mantle. The first method, Dz (from Dziewonski[4]), involves expressing velocity perturbations δV in terms of smooth functions—Legendre functions in radius r and spherical harmonics in colatitude θ and longitude φ:

$$\delta V(r, \theta, \varphi) = \sum_{k=0}^{K} \sum_{l=0}^{L} \sum_{m=0}^{l} f_k(r) \cdot ({}_kA_l^m \cos m\varphi + {}_kB_l^m \sin m\varphi) P_l^m(\cos \theta)$$

Some 500,000 travel-time residuals for teleseismic arrivals from 5,000 earthquakes were used in an iterative least-squares procedure to derive the coefficients A and B for $K = 4$ and $L = 6$ for 245 coefficients.

The second tomographic method (CC, from Clayton and Comer[5,6]) is an iterative back projection of travel-time residuals along ray paths. The mantle is discretized into 29 spherical shells, each 100-km thick, with each shell divided into 1,676 cells ~500 km on a side. At every iteration, the slowness $(1/V)$ perturbation, δS_i, in the ith cell is incremented by

$$\frac{\sum_{k=1}^{M} (l_{ki}\delta t_k / L_k)}{\mu + \sum_{k=1}^{M} l_{ki}}$$

where, for the kth ray, δt_k is the residual relative to the preceding iteration, L_k is the total ray length, l_{ki} is the ray length in the cell (which may be zero), M is the total number of rays and μ is a damping parameter. The procedure converges to the smallest δS_i in the sense of a Euclidean norm, where the cells intersected by more rays are given greater significance than others, that minimizes

$$\sum_{k=1}^{K} \left[\left(\delta t_k - \sum_{i=1}^{N} l_{ki}\delta S_i \right)^2 \Big/ L_k \right]$$

Here, N is the total number of cells, K is the total number of rays and δt_k is a residual relative to the (spherically symmetric) starting model.

Each inversion method has advantages and disadvantages. Method Dz gives a direct global inversion for the long wavelength features of interest for comparison with the geoid and provides a resolution matrix with formal uncertainties. It is a low-order polynomial fit to sparse data, allowing model

* Present addresses: Department of Earth and Space Sciences, State University of New York, Stony Brook, New York 11794, USA (R.P.C.); Department of Geological Sciences, Harvard University, Cambridge, Massachusetts 02138, USA (A.M.D.).

excursions in regions not well constrained by data and not allowing rapid radial variation of the model. Method CC allows determination of finer structure and provides a simple visualization of those regions not covered by rays, making it easy to see regions that are not constrained by observations. It does not, however, provide formal uncertainties. Because it is expanded ultimately in terms of spherical harmonics for comparison with the gravity field, it shares the problem of how best to interpolate into regions not well constrained by observations. We derive the spherical harmonic expansion coefficients used here with a least-squares fit to the blocks in a given layer.

At this stage, the primary limitations for both approaches are the non-uniform distribution of ray coverage brought about by both the uneven distribution of sources and receivers and noise in the travel-time data. It is encouraging that the two methods agree in the longest-wavelength components of velocity anomalies ($l = 2$–3), although the agreement is poor at shorter wavelengths ($l \geqslant 4$). We confine our interpretation to those wavelengths where the methods agree, justified in part by the fact that at these wavelengths the seismic models can predict the geoid if dynamic effects are taken into account properly.

Generation of geoid anomalies

Although on short time scales the mantle behaves as an elastic solid, it is recognized commonly that on geological time scales it behaves as a viscous fluid, responding to stresses by slow creeping flow. Less commonly recognized is that the flow resulting from interior density contrasts (such as those inferred from studies of variations in seismic velocity) leads to deformation of the Earth's surface, the core–mantle boundary and any other boundary in chemical composition which may exist in the mantle[7–9]. This boundary deformation occurs on the same time scale as postglacial rebound, short compared with the time it takes for the position of the interior density pattern to change appreciably[8]. Thus, boundary deformation can be taken to occur instantaneously from the standpoint of mantle convection.

The total geoid anomaly observed at the surface is the sum of the opposing effects of the interior density contrasts driving the flow and the mass anomalies caused by boundary deformations resulting from the flow. The amplitudes of the boundary deformations, and hence the sign and magnitude of the total geoid anomaly, depend on the distribution of viscosity with depth and the presence or absence of chemical stratification[8–10].

We use spherical harmonics to describe the gravity field, as well as the seismic velocity heterogeneities. Given the spherical harmonic coefficient of density perturbation as a function of radius, $\delta\rho_l^m(r)$, the total gravitational potential U_l^m is given by the integral:

$$U_l^m = \frac{4\pi\gamma a}{2l+1} \int_c^a G_l^m(r)\delta\rho_l^m(r)\,\mathrm{d}r \qquad (3)$$

Here, γ is the gravitational constant, a is the radius of the Earth, c the radius of the core and $G_l^m(r)$ is the dynamic response function or kernel[8–10]. This kernel includes the contributions of the boundary deformations caused by the flow induced by $\delta\rho_l^m(r)$, as well as from the driving density contrast itself.

We calculate dynamic response functions using models that treat the mantle as an incompressible newtonian fluid with a spherically-symmetric viscosity structure. The m dependence of G is then degenerate and G is a function of l and r only. Both the viscosity structure and the intrinsic density profile due to differences in chemical composition can be layered. Phase changes in a layer of uniform composition are assumed to have negligible effect on the flow field, as phase changes by themselves do not present a barrier to radial flow. (Any horizontal density contrasts arising from phase changes are, at least in principle, part of the seismically-inferred density field.)

Free-slip boundary conditions are applied at the Earth's surface and at the core–mantle boundary. At boundaries between layers of the same chemical composition but differing viscosities, velocities and tractions are continuous. At boundaries between
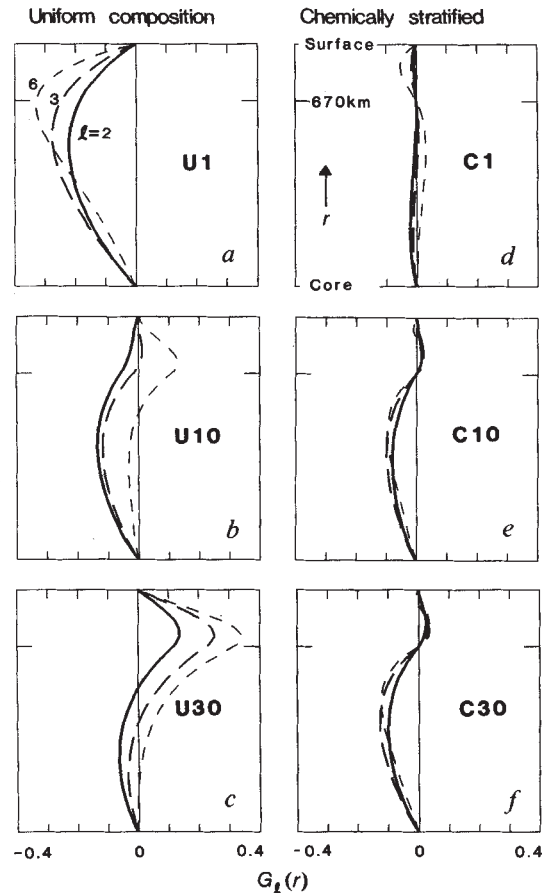

Fig. 1 Dynamic response functions for surface density contrasts of spherical harmonic degrees 2 (solid lines), 3 (long dashes), and 6 (short dashes) plotted against radius for six Earth models. Models U, left, have uniform composition which permits mantle-wide flow; models C, right, have a chemical discontinuity at 670-km depth, causing stratification into separate upper and lower mantle flow systems. Models in the top row have uniform viscosity; those in the middle row have a factor of 10 viscosity increase below 670 km. This viscosity increase is a factor of 30 for models in the bottom row.

layers of differing chemical compositions, radial velocities are set to zero, prohibiting radial flow between layers. Other velocity components and tractions are continuous, leading to separate flow systems with shear coupling across the boundary.

Our assumption of a newtonian, spherically-symmetric viscosity distribution is done for the sake of mathematical tractability and to provide a simple model of the relevant physics. The viscosity of mantle rocks depends on both temperature and stress[11]; lateral variations in viscosity are expected to accompany the observed lateral heterogeneity in seismic velocity. The existence of tectonic plates (which translate as nearly rigid blocks) with deformation concentrated in zones of weakness at plate boundaries, demonstrates that lateral viscosity variations are important in the Earth. Our primary justification for using such simple models is that they are adequate to explain the longest-wavelength components of the geoid. The main effect of long-wavelength lateral variations in viscosity is to excite flow at shorter wavelengths, leaving the geoid signature at the long wavelengths relatively unaffected[12].

Examples of dynamic response functions $G_l(r)$ for six simple viscous Earth models are shown in Fig. 1 for spherical harmonic degrees 2, 3 and 6. U1, U10 and U30 in the left column represent mantle models of uniform composition with a ratio of lower-mantle to upper-mantle viscosity of 1, 10 and 30 respectively. (Although flow velocities depend on the actual value of viscosity chosen, stresses and geoid anomalies depend only on the relative distribution of viscosity.) Models C1, C10 and C30 in the right
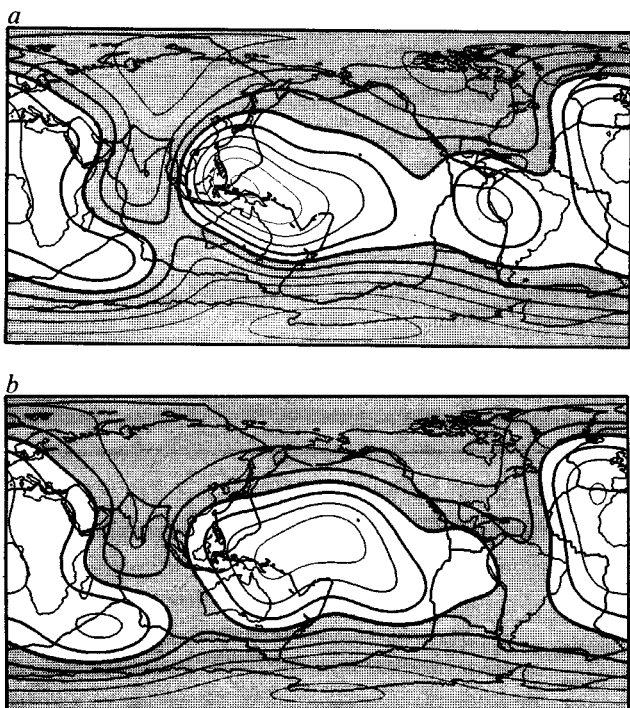
Fig. 2 *a*, The observed geoid[13] for *l* = 2–6 referred to the hydrostatic figure of the Earth. Geoid lows are shaded and the contour interval is 20 m. In all our maps, we show plate boundaries and continents for reference. *b*, The residual geoid for *l* = 2–6 obtained by subtracting the effects of subducted slabs[10]. Lows are shaded; the contour interval is 20 m.
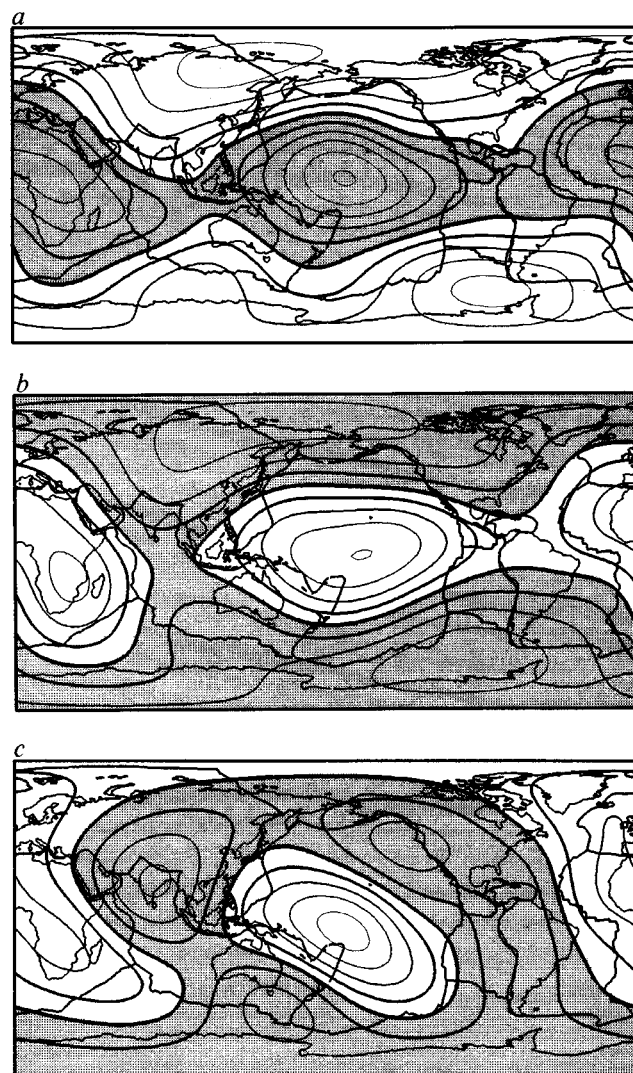

Fig. 3 Geoids calculated by applying dynamic response functions, such as those in Fig. 1, to the seismic models. *a*, CC–S, a static model (boundary deformation is not included); contour interval, 50 m. *b*, CC–U10, for a uniform composition model with a factor of 10 increase in lower mantle viscosity. *c*, Dz–U10, as *b*; contour intervals, 20 m. Lows are shaded.

column are for models with an intrinsic chemical density contrast at 670-km depth, with separate flow systems above and below the 670-km seismic discontinuity. The viscosity structure for these models is identical to that in the corresponding row for the uniform composition models.

For a given density contrast, the magnitude and sign of the resulting geoid anomaly in a dynamic Earth depends on the viscosity structure. For example, in model U1, the opposing gravitational effect of deformation of the upper boundary overwhelms that of the interior density contrast itself, leading to a negative geoid anomaly for a positive density contrast. For model U30, because of the strong increase in viscosity with depth, most of the deformation occurs at the core–mantle boundary, further away from the observer than the density anomaly driving the flow. The effect of the density contrast dominates and the response function is more positive. The net gravitational field of a dynamic Earth is a small number determined by the difference of larger, nearly counter-balancing quantities. The sign of the field depends on which of the effects is dominant. The anomaly may depend also on the depth of the convecting system, with chemically stratified systems leading usually to smaller geoid anomalies for a given density anomaly. Observations of both the geoid and seismic velocity heterogeneities over a range of wavelengths place constraints on the variation of mantle viscosity and the depth of mantle convection. Observation of dynamic surface deformation provides a complementary constraint.

Results

Figure 2*a* shows a recent long-wavelength (*l* = 2–6) geoid[13], referred to the hydrostatic equilibrium figure[14], superimposed on a map including plate boundaries. There is a strong association of geoid highs with subducted slabs[10,15–17] but there is much variation, particularly at the longest wavelengths, not associated with the present plate configuration.

This can be seen more clearly in Fig. 2*b*, a residual geoid determined by subtracting from the observed geoid slab effects obtained using a mantle flow model in conjunction with a model of the density structure of subducted slabs[10]. This flow model assumes mantle-wide flow and an upper mantle with a viscosity 0.01 times that of the lower mantle. Other more empirical studies give similar residual geoids[16,17]. The residual geoid has a poolball like pattern dominated by antipodal highs over north-west Africa and the central Pacific. The highs are in regions shielded from subduction for substantial parts of the recent geological past and might be expected to represent hotter than average mantle[18,19]. Indeed, there is a strong correlation between long-wavelength residual geoid highs and hotspots[16,17].

These geoids can be compared with model geoids calculated using the lower-mantle seismic models. Velocity and density perturbations are assumed to be directly proportional and the seismically inferred density anomalies are convolved with the response functions shown in Fig. 1, as well as those for a static (rigid) Earth. If dynamic surface deformation is ignored (Fig. 3*a*, model CC–S, for static), the geoid anomaly matches the pattern, in general, but is of opposite sign to the observed or residual geoids. Thus, we must consider the gravitational effects of surface deformation.

For uniform composition and viscosity (model U1, not shown) there is general agreement between the calculated and the residual geoids, but the high-frequency component has too great an amplitude in the calculated geoid and the best fitting proportionality constants for degrees 2 and 3 differ substantially. For model U10, with uniform composition and a lower mantle viscosity increased by a factor of 10, there is an excellent correlation between the calculated and residual geoids at longest wavelengths for either model CC (Fig. 3b) or model Dz (Fig. 3c). This agreement breaks down for model U30, which has a factor of 30 increase in lower mantle viscosity.

For the chemically layered model C1, the agreement is poor. Models C10 and C30 predict geoids similar to each other (seen by comparing the response functions in Fig. 1e and f). Either provides a good match to the residual geoid, almost as good as model U10. The general agreement between models U10 and C10 (and C30) is expected from the similarity of their response functions at $l = 2$-3, Fig. 1b and 1e.

Correlation coefficients for degrees 2-6 are given in Table 1 for the observed geoid, the residual geoid and models Dz-U10 and CC-U10. For both models, the agreement at $l = 2$-3 is excellent, with the best fitting proportionality constant about $(4 \text{ km s}^{-1})/(\text{g cm}^{-3})$, close to that predicted for likely mantle compositions and observed for variations in velocity and density with radius near the top of the lower mantle[20]. The positive correlation is consistent with the convection hypothesis, with both high velocities and high densities associated with cold material.

The dynamically maintained topography at the Earth's surface and at the core-mantle boundary for degrees 2-3, calculated for model CC-U10, is shown in Fig. 4. Both the core-mantle boundary and the surface are upwarped in regions of low seismic velocity and downwarped in regions of high velocity (and presumably high density). These dynamically induced deformations of the top and bottom of the convecting system represent substantial mass anomalies. Their effects on the geoid are so large that they overwhelm the effects of the internal density contrasts driving the flow, thereby determining the sign of the geoid.

The total geoid is correlated positively with dynamic surface deformations and negatively with seismically inferred density anomalies. This confirms the need to consider the effects of dynamic surface deformation in calculating geoid anomalies; neglecting it leads to an error in sign as well as in magnitude.

Because the gravitational response functions for flow models U10 and C10 are so similar, it is not possible to discriminate between these two models using only the longest-wavelength geoid predicted from our present models of seismic heterogeneity in the lower mantle. However, these two models predict quite different values for the dynamically maintained topography at the Earth's surface. The dynamic surface topography predicted for the chemically stratified model CC-C10 is quite similar in pattern to that for model CC-U10, Fig. 4a. However, it is of opposite sign due to the shear coupling of flow between the upper and lower mantle in a chemically stratified mantle, and is a factor of three lower in amplitude. If it were possible to strip out the isostatic effects of crustal thickness variations and the dynamic effects of upper mantle heterogeneity to isolate the dynamic component of surface topography due to lower-mantle density anomalies, it would be possible to distinguish between these models.

An accurate determination of the long-wavelength component of dynamic topography requires a knowledge of the global distribution of crustal densities and thickness variations, beyond the scope of this report. If we assume, however, that depth or elevation anomalies in similar tectonic provinces are due to dynamic surface deformation, we can begin to compare Fig. 4a with some observations. Comparing ancient shield regions which have been unaffected by crustal thickening in the last billion years (and might, therefore, have been eroded to the same elevation), we find that Africa stands higher than the Canadian or Siberian shields by several hundred metres[8]. There is a broad
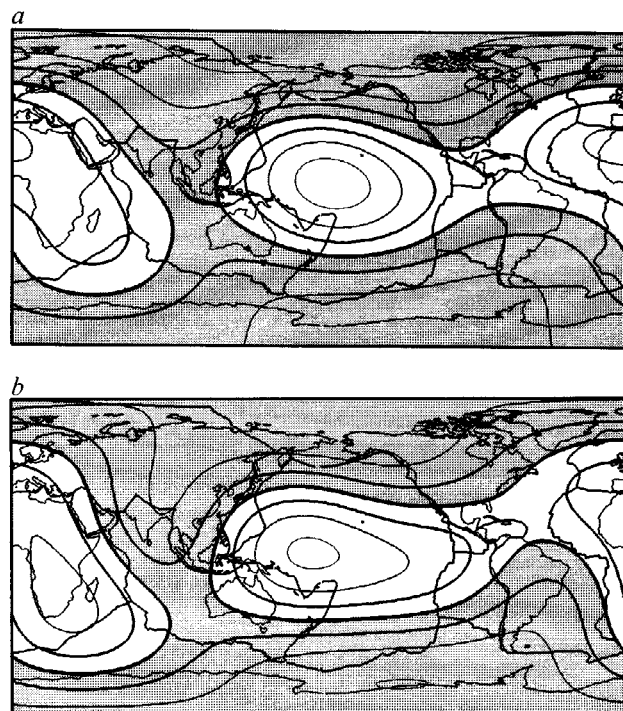
Fig. 4 Calculated topography for $l = 2$-3, a, at the surface and b, core-mantle boundary for the model CC-U10, which matches the geoid. Surface topography was calculated assuming a density contrast of 2.3 g cm^{-3} (appropriate for sub-oceanic regions). Topography at the core-mantle boundary is calculated for a density contrast of 4.5 g cm^{-3} across the interface. Lows are shaded. Contour intervals: a, 250 m; b, 500 m.

region of anomalously shallow (250-750 m) sea floor in the Western Pacific and an anomalously deep (> 500 m) region south of Australia[21]. Africa is surrounded mainly by anomalously shallow seafloor. Comparing long-wavelength model predictions with a spotty and possibly aliased distribution of points on a map is dangerous. But we find that the agreement of our uniform-composition model predictions with what is known of the distribution of residual topographic anomalies, and the disagreement with the predictions of the chemically stratified model, suggest mantle-wide convection.

Temporal variations in large amplitude, dynamically-maintained surface topography would contribute to epeirogeny and eustatic sea-level changes. For example, changes in the positions of continents and ocean basins relative to the underlying convection pattern itself could explain easily the range of eustatic sea-level changes observed. Records of 'eustatic' sea level from different continents would depend on their positions relative to the long-wavelength mantle flow pattern.

Dynamically maintained topography at the core-mantle boundary has a total excursion of ~ 3 km for either model. Such large topography has been suggested as influencing the geodynamo[22] and may be important in coupling nutation of the mantle to the core. The dynamic topography for degrees 2-3 is a substantial fraction of the 9-km topography due to the hydrostatic ellipticity of the core-mantle boundary. Higher-degree terms are expected to increase the dynamic topography substantially.

Discussion

There is remarkable agreement between the residual geoid and the geoid calculated using the dynamic response functions for models U10 or C10 using either seismic model. The agreement between the predictions of either seismic model and the geoid is comparable with the agreement between the two seismic models. Using the seismic models (and the dynamic slab

model[10]) we can explain more than 80% of the variance in the observed $l = 2-3$ geoid. This agreement is unlikely to be due to chance.

There are certainly large heterogeneities in the upper mantle which might be expected *a priori* to mask the signal from the lower mantle. For example, several seismic studies have reported a degree 2 velocity anomaly in the upper mantle which correlates well with the degree 2 geoid[23-25]. It is remarkable that the fit of the geoid is so good, as we have neglected upper mantle contributions. The longest-wavelength dynamic response functions for our successful models (U10 or C10), however, are quite small in the upper mantle. The $l = 2-3$ geoid is not as sensitive to density anomalies there as it is to those in the lower mantle; the effects of heterogeneities in the transition zone are compensated almost totally by surface deformation.

The seismic results show that at degrees 2-3, geoid lows are associated with fast lower mantle whereas highs are associated with slow lower mantle. We suggest that these velocity variations are caused by temperature differences of convective origin. This interpretation is supported by a very high correlation ($r > 0.99$) between the degree 2 distribution of hotspots and the radially-averaged degree 2 lower mantle seismic velocity anomalies. This supports the hypotheses that geoid lows result from areas where subduction has cooled the mantle[19] and that shielding of the mantle by continents results in geoid highs and hotspots[18]. Mantle-wide flow provides a simple explanation for the fact that hotspot provinces at the surface tend to overly the long-wavelength expression of hot lower mantle. The relatively higher viscosity we find for the lower mantle may help to explain the long time scales inferred to be associated with these phenomena.

We have confined our analysis here to fairly simple viscosity distributions that, nonetheless, have allowed us to explain most of the variance in the longest-wavelength components of the geoid. The viscosity models presented are not unique; viscosity values should be regarded as weighted averages over the two layers used. We can provide even better matches to the geoid using more complicated viscosity models, including, for example, a low viscosity channel beneath a high viscosity layer representing a lithospheric lid. The best two-layer viscosity model used in fitting the seismic results to the residual geoid has a smaller viscosity contrast between the upper and lower mantle than the two-layer model used to isolate and remove slab effects[10], consistent with the lithosphere or upper mantle having a lower effective viscosity at plate boundaries than in plate interiors. It is possible, however, using a uniform composition model with four viscosity layers, to achieve a self-consistent spherically symmetric model for both the inferred lower mantle density anomalies and subducted slabs (B.H.H., in preparation).

Finally, although the agreement at long wavelengths is impressive, the agreement at $l \geqslant 4$ between the predictions of these models and the geoid is not good. This is in part the result of oversimplification in the flow models, which contain only two layers and which assume a spherically symmetric effective viscosity. On the other hand, the disagreement between the seismic methods at $l \geqslant 4$ leads to the hope that improved seismic data (such as will be provided by the proposed Global Seismic Array) and new techniques for its analysis, as well as including results for upper mantle heterogeneity, will yield an understanding of the geoid at shorter wavelengths. The insights into mantle dynamics provided by even these relatively coarse seismic studies are extremely valuable. Further cooperative studies by seismologists and geodynamicists should lead to even better constraints on the dynamics of convection in the Earth's mantle.

1. Kaula, W. M. *J. geophys. Res.* **68**, 473-484 (1963).
2. Guier, W. H. *Nature* **200**, 124-125 (1963).
3. Dziewonski, A. M., Hager, B. H. & O'Connell, R. J. *J. geophys. Res.* **82**, 239-255 (1977).
4. Dziewonski, A. M. *J. geophys. Res.* **89**, 5929-5952 (1984).
5. Comer, R. P. & Clayton, R. W. *J. geophys. Res.* (submitted).
6. Clayton, R. W. & Comer, R. P. *J. geophys. Res.* (submitted).
7. Pekeris, C. L. *Mon. Not. R. astr. Soc. Geophys. Suppl.* **3**, 343-367 (1935).
8. Richards, M. A. & Hager, B. H. *J. geophys. Res.* **89**, 5987-6002 (1984).
9. Ricard, Y., Fleitout, L. & Froidevaux, C. *Annls Geophys.* **2**, 267-286 (1984).
10. Hager, B. H. *J. geophys. Res.* **89**, 6003-6015 (1984).
11. Ashby, M. F. & Verrall, R. A. *Phil. Trans. R. Soc.* **A288**, 59-95 (1977).
12. Richards, M. A. & Hager, B. H. *EOS* **65**, 1092 (1984).
13. Lerch, F. J., Klosko, S. M. & Patch, G. B. *LAGE05(GEM-L2)* (NASA Technical Memorandum, 84986, 1983).
14. Nakiboglu, S. M. *Phys. Earth planet. Inter.*, **28**, 302-311 (1982).
15. Kaula, W. M. *The Nature of the Solid Earth* (ed. Robertson, E. G.) 385-405 (McGraw-Hill, New York, 1972).
16. Chase, C. G. *Nature* **282**, 464-468 (1979).
17. Crough, S. T. & Jurdy, D. M. *Earth planet. Sci. Lett.* **48**, 15-22 (1980).
18. Anderson, D. L. *Nature* **297**, 391 (1982).
19. Chase, C. G. & Sprowl, D. R. *Earth planet. Sci. Lett.* **62**, 314-320 (1983).
20. Bass, J. D. & Anderson, D. L. *Geophys. Res. Lett.* **11**, 237-240 (1984).
21. Crough, S. T. *A Rev. Earth planet. Sci.* **11**, 165 (1983).
22. Malin, S. R. C. & Hide, R. *Phil. Trans. R. Soc.* **A306**, 281 (1982).
23. Masters, G., Jordan, T. H., Silver, P. G. & Gilbert, F. *Nature* **298**, 609-613 (1982).
24. Woodhouse, J. & Dziewonski, A. M. *J. geophys. Res.* **89**, 5953-5986 (1984).
25. Nakanishi, I. & Anderson, D. L. *Nature* **307**, 117-121 (1984).

Segmental distribution of bithorax complex proteins during *Drosophila* development

Philip A. Beachy*, Stephen L. Helfand† & David S. Hogness*

Departments of *Biochemistry and †Biological Sciences, Stanford University School of Medicine, Stanford, California 94305, USA

The Ubx and bxd transcription units comprise a single functional domain in the bithorax complex of Drosophila melanogaster. The segmental distributions and nuclear localization of proteins encoded by the Ubx unit have been determined by immunofluorescence staining with antibodies raised against a fusion protein containing Ubx coding sequences. Wild-type and mutant distributions are consistent with a model in which the protein-coding functions of the domain derive from the Ubx unit and are regulated by the bxd unit.

THE metazoan genome faces a unique set of demands in its task of directing the complex process of multicellular development. Not only must the characteristics of individual cells be specified, but also the size, shape and other higher-order characteristics of the multicellular structures they constitute. In *Drosophila melanogaster*, the body plan of both larva and fly is characterized by a series of segments whose identities vary according to position along the anterior-to-posterior axis of the animal. The role genes play in the specification of these identities has been defined, in part, by homoeotic mutations that produce specific intersegmental transformations of identity by causing embryonic founder cells at one position to adopt the fates reserved normally